Si-integrated ferroelectrics for photonics and optical computing

Alexander A. Demkov* and Agham B. Posadas

The von Neumann computer architecture is experiencing difficulties with both scaling and power consumption requirements, and as a result, new computing paradigms are being actively explored. Even more revolutionary would be a complete or partial switch from electrons to photons. Infrared silicon photonics is one possible avenue for realizing such an alternative computing paradigm. This technology will ultimately require integration of active and passive photonic elements on a single chip. One key photonic element is an optical modulator. Here, we summarize the recent progress in integrating ferroelectric $LiNbO_3$ and $BaTiO_3$ with silicon photonics for the purpose of fabricating electro-optic modulators exploiting the linear electro-optic effect.

Introduction

Despite its phenomenal success for nearly half a century, modern computing based on the von Neumann architecture, as implemented in planar complementary metal–oxide–semiconductor (CMOS) technology, is showing signs of aging and fatigue. Though the device scaling that drives Moore's Law still persists, computer clock speeds have been stuck at about 3 GHz for well over a decade.[1] Part of the problem lies in the RC delay of the back-end metal layers that provide intra-chip connections. Another problem is that of power consumption and heat dissipation, the latter being exacerbated by the industry switch to silicon-on-insulator or SOI technology. The development of multi-core architectures only increased the amount of data one needs to move around the chip, causing further power issues. In the von Neumann architecture, the central processing unit (CPU) and memory are two distinct elements, and the data rate between them is lower than the rate of the CPU itself, creating the so-called von Neumann bottleneck. In the biological brain, storage and processing are done in the same place; emulating this architecture amounts to neuromorphic or brain-like computing. The rise of neuromorphic computing and artificial intelligence is an attempt to overcome the limitations of the von Neumann architecture, but it is still being implemented using electronic devices and the problems do not stop at the chip's edge. Inter-chip communications or interconnects hit the bandwidth wall at frequencies above 40 GHz, at which point the copper lines behave similar to very lossy waveguides.[2]

Potentially, all these woes can be alleviated if one were to switch from electronic to optical signals. Optical computing is not a particularly new topic, but historically, it was discussed in terms of free space optics or, in the case of telecommunications, in terms of the optical fiber. Both purely optical and hybrid optoelectronic approaches have been considered. The intrinsic parallelism of optics makes it a natural medium for implementing neuromorphic as well as quantum computing algorithms.

That promise is at the heart of the unprecedented interest in silicon photonics. Silicon is essentially transparent at a wavelength of 1.55 μm and can therefore serve as a bridge between optical fiber telecommunications and chip-integrated devices known as photonic integrated circuits or PICs. The relatively large size of integrated active optical structures (about 500 μm) was often used against them when compared with conventional transistors. One can place many more transistors on the same real estate. This calculus changed when neuromorphic computing entered the picture. One no longer needs to represent Boolean logic with simple switches. That and the

Alexander A. Demkov, Department of Physics, The University of Texas at Austin, Austin, USA; demkov@physics.utexas.edu
Agham B. Posadas, Department of Physics, The University of Texas at Austin, Austin, USA; agham.posadas@utexas.edu

doi:10.1557/s43577-022-00332-3

fact that existing Si manufacturing can still be used make Si photonics extremely attractive not only as interconnects but as a computing platform in its own right.[3,4]

One of the potential issues with Si PICs is the need for heterogeneous integration. Silicon itself is an excellent waveguide material but is not very useful for light sources or detectors. Those are fabricated in III–V materials and Ge, respectively. But even modulators, the optically active elements of the chip, are still essentially electronic devices. Thus, even though Si offers a very convenient platform for basic optical elements such as waveguides, beam splitters, directional couplers or delay lines, simple electro-optic (EO) modulators such as Mach–Zehnder modulators (MZMs) present a potential problem.

EO modulation can be achieved in III–V semiconductor devices. The typical EO device in III–V systems is an electroabsorption modulator. The EO effect in this class of materials arises from a combination of a weak linear electro-optic or Pockels effect (coefficient of −1.6 pm/V for GaAs) and the Franz–Keldysh effect, which is a change in absorption of near band-edge wavelengths due to broadening and shifting of the band edge under an applied electric field. This effect can be enhanced through the quantum-confined Stark effect that occurs in multiple quantum well heterostructures. The higher refractive index of III–V semiconductors (−3) can partially compensate for the weak Pockels coefficient, but in order to be compatible with Si photonics, a complicated and costly wafer bonding process to a fully processed silicon-on-insulator (SOI) wafer is required.[5]

In response to this challenge, there has been significant research activity in optical modulators that utilize advanced materials that can be more readily integrated with Si.[6] Among these novel materials systems, ferroelectrics offer a particularly elegant solution. Oxides such as $LiNbO_3$ and $BaTiO_3$ exhibit a significant linear electro-optic or Pockels effect, that is, when a large electric field is applied, the speed of light propagation in the material changes. This effect is quantified by the Pockels coefficient, which is proportional to the change in the refractive index for a given external electric field and has units of inverse electric field. In other words, the refractive index is a linear function of the applied electric field. This offers a simple way to fabricate phase shifters that, being field operated, require energy only to charge the relevant capacitor. The Pockels effect also offers one of the fastest switching mechanisms. A typical Mach–Zehnder Pockels phase shifter is a waveguide fabricated in an electro-optically active material and placed between two electrodes. The field is determined by the applied voltage V and the distance between the electrodes d; the change of the refractive index is proportional to a product of this field and $\boldsymbol{r}$, a linear combination of components of the Pockels tensor that is determined by the relative geometric arrangement of the ferroelectric polarization, electrodes and direction of light propagation. The total phase shift is proportional to the product of the index change and the length of the modulated region, specifically $\Delta\varphi = n^3 \frac{\pi}{\lambda} r \frac{V}{d} L$, where n is the index of refraction, L is the length of the electrode, and λ is the wavelength. The efficiency of an MZM is typically quantified by the so-called half-wave voltage–length product $V_\pi L$, which is the voltage needed to shift the phase of an optical signal by π multiplied by the length of the device. The smaller the number, the more efficient the device and values below 1 V·cm are typically desirable for photonic integrated circuits.

The physics of the Pockels effect lies in subtle changes a strong electric field can produce in a material. Being linear in the electric field, the effect requires the absence of inversion symmetry, which excludes bulk silicon. First, the field would change the band structure that, in turn, will affect electronic polarizability. This mechanism is responsible for effects such as second-harmonic generation and is quantified by the second order electronic susceptibility $\chi^{(2)}$. Electronic response is present across a broad frequency spectrum but is modest. Second, in an ionic oxide, the field would shift ions from their equilibrium positions; this change in the atomic geometry would also change the band structure that, in turn, will also affect the electronic polarizability. This mechanism is also behind Raman scattering, and the large Raman polarizability (derivative of the electronic susceptibility with respect to atomic displacement and a measure of the electron–phonon interaction), combined with low frequency phonon modes results in a large electro-optic effect. The electro-optic response is proportional to Raman polarizability and inversely proportional to the square of the phonon frequency. It is driven by optical phonons and is present below the acoustic resonance up to the THz range of the spectrum. Third, in piezoelectric crystals, a strong electric field causes a lattice deformation that, in turn, changes the band structure and further affects the electronic polarizability. This is a low frequency response of the system controlled by the acoustic phonons. Below 10 GHz all three mechanisms are present, and we talk about the unclamped electro-optic response. Above this frequency we deal instead with the clamped response, when only the electrons and optical phonons contribute. Ultimately, at a very high frequency, only the electronic component contributes to the electro-optic effect. In $LiNbO_3$ and $BaTiO_3$ we find a robust electro-optic effect, described by components of the third rank Pockels tensor (it relates the second rank dielectric tensor with the electric-field vector). The largest components of the unclamped Pockels tensor are 36 and 1300 pm/V in $LiNbO_3$ and $BaTiO_3$, respectively.

Most importantly, both $LiNbO_3$ and $BaTiO_3$ can be integrated with Si. $LiNbO_3$ requires wafer bonding, while $BaTiO_3$ can be directly integrated on an 8-in. Si wafer using conventional deposition techniques, such as molecular beam epitaxy, chemical vapor deposition, or RF sputtering. In what follows, we will briefly describe the deposition techniques and recent results of fabricating electro-optic devices based on Si-integrated ferroelectrics.

Deposition methods

The direct epitaxial integration of the perovskite oxide $SrTiO_3$ on Si, first reported by McKee et al.,[7] is the key technology that allows $BaTiO_3$ to be simply integrated with Si by

conventional thin-film deposition. Currently, the direct epitaxy of $SrTiO_3$ on Si requires the use of molecular beam epitaxy (MBE) in order to keep unwanted Si oxidation under control.[8] However, recent efforts at using pulsed laser deposition (PLD) to perform the direct epitaxy have been demonstrated to work as well.[9] With a $SrTiO_3$ layer in place on Si, other perovskite oxides, including $BaTiO_3$, can readily be grown in single crystal, epitaxial form using standard deposition processes.

Chemical vapor deposition (CVD) is a process that forms solid thin films of a material from gaseous species that react on the surface of a heated substrate. CVD processes are known for their versatility and very high growth rates.[10] The use of CVD for depositing epitaxial oxides came into prominence during the height of the high-T_c superconductor discovery. In the case of $BaTiO_3$, the variant of CVD known as metal–organic CVD (MOCVD) is the most used. One disadvantage of MOCVD is that the reactions are endothermic, and energy must be supplied to sustain the reaction. This has traditionally been done by heating the substrate, often to quite high temperatures (>800°C). This has led to the development of other methods of providing energy to the reactants, most notably by creating a plasma leading to the technique known as plasma-enhanced CVD (PECVD).[10] Other drawbacks of CVD are the need for more complicated gas distribution systems and the need to develop suitable precursor compounds. Pioneering work for making $BaTiO_3$ electro-optic devices using MOCVD was reported in 2004 by the Wessels group at Northwestern University. They grew a 570-nm $BaTiO_3$ film on MgO single-crystal substrate using titanium isopropoxide and a fluorinated Ba precursor ((Ba(hfa_2)-PEB), with oxygen as oxidant and argon as carrier gas. They used a two-step process with an initial nucleation at 750°C for 5 min and the main growth at 900°C. The reported growth rate was 5.0–6.7 nm/min.[11] Strip waveguides of 125-nm-thick Si_3N_4 with width of 4 μm and 3.2 mm in length were patterned on top of the $BaTiO_3$ film with coplanar Cr/Au electrodes having a gap of 8 μm. Electro-optic modulation of the waveguide shows a $V_\pi L$ of 1.1 V·cm and an effective Pockels coefficient of 162 pm/V.[12]

Atomic layer deposition (ALD) is a special variant of the CVD process that involves alternating self-limited surface reactions of a precursor chemical with the substrate. Excess precursor and reaction byproducts are purged after each subcycle prior to the next subcycle.[10] For growing complex oxides like $BaTiO_3$, one needs a precursor for each element. The oxygen precursor in ALD is most often water, and each ALD cycle consists of a Ba pulse, water pulse, Ti pulse, and a second water pulse, with purging steps in between each pulse. The cycle is repeated as many times as needed to grow the desired film thickness. Epitaxial growth of $BaTiO_3$ on Si by ALD was first reported by Ngo et al.[13] The film was deposited at 225°C but requires an anneal at 600°C to fully crystallize the film. The precursors used were barium bis(triisopropylcyclopentadienyl) and titanium tetraisopropoxide. The annealing process was found to be able to control the crystallographic orientation of the $BaTiO_3$ depending on the cooling rate. The ALD process is quite slow for complex oxides and the effective growth rate reported by Ngo et al. is less than 0.09 nm/min. Lin et al. measured the electro-optic properties of $BaTiO_3$ grown using this process in a transmission geometry. $BaTiO_3$ films on Si with 40-nm thickness and *a*-axis orientation having patterned tungsten top electrodes (gap of 5 mm) at various orientations were used for the measurement. For an electric field applied in the $\langle\langle 110 \rangle\rangle$ direction, the film showed an effective Pockels coefficient of 26 pm/V.[14] The low value of the Pockels response is likely due to a combination of the small film thickness[15] used and the columnar microstructure of ALD grown perovskite films, which results in some voids.

Sol-gel deposition (also known as chemical solution deposition) is another chemical means of depositing thin films. It involves dissolving precursor compounds in a solution and then driving out the solvent. The material is then calcined to form the final oxide layer. The process is repeated several times to get to the desired thickness. Sol-gel is known for its low cost, especially in terms of equipment but it does suffer from relatively low structural quality of films.[16] Edmonson et al. grew epitaxial $BaTiO_3$ on Si using this process. They used barium acetate and titanium isopropoxide as precursors, dissolved in glacial acetic acid. The solution is spun onto the $SrTiO_3$-buffered Si and pyrolyzed at 400°C. The sample is then crystallized in flowing oxygen at 600°C for 1 h.[17] The film electro-optic response was measured in a transmission geometry for a 90-nm film, and they found that the effective Pockels coefficient is 27 pm/V. However, annealing the films a second time at 750°C for 10 h in flowing oxygen increases the electro-optic response to 89 pm/V. This again highlights the importance of good film microstructure to obtaining higher electro-optic response.

MBE involves the thermal evaporation of elemental sources under ultrahigh vacuum conditions. The combination of low base pressures (typically -10^{-10} Torr) and specialized evaporation sources known as effusion cells results in the evaporated material taking the form of atomic beams directed at the substrate, which can be quickly turned on and off through the use of shutters.[18] The flux of atoms is controlled by the temperature of the effusion cell. For the growth of oxides, a source of oxygen is needed, either molecular oxygen or an active oxygen species like ozone or atomic oxygen from a plasma source. Flux is most often measured using either a quartz crystal microbalance or a nude ion gauge to measure beam equivalent pressure. For $BaTiO_3$ growth, one uses metallic Ba and Ti as the metal sources, with molecular oxygen being sufficient to produce high-quality films. The evaporation of Ti is somewhat difficult due to its low vapor pressure. One needs a special high-temperature cell in combination with a crucible that can hold liquid Ti. The Ti flux typically limits the rate at which one can grow $BaTiO_3$ by MBE. Typical MBE growth conditions use a substrate temperature of 700°C with a total growth rate of 0.2–0.4 nm/min at an oxygen pressure of ~5×10^{-6} Torr. To achieve these rates, the Ba effusion cell is operated around 575–600°C while the Ti effusion cell is

operated around 1725–1750°C MBE-grown $BaTiO_3$ electro-optic devices integrated on Si have been fabricated in the last couple of years, with some of the highest effective Pockels coefficients reported for electro-optic modulators,[19] which will be discussed in more detail below. This is a testament to the extremely high crystalline quality of films that can be achieved with MBE, whose main drawback is the slow deposition rate along with flux drift over time.

Pulsed laser deposition (PLD), sometimes referred to as laser ablation or laser MBE, is a method of thin-film deposition that uses a series of high-energy laser pulses to rapidly vaporize a source material known as a target, which is typically a bulk material with the same composition as the film to be grown. Under optimized conditions, PLD has the ability to stoichiometrically transfer the composition of the target to the growing film, alleviating the need for precise individual elemental flux control as with MBE. The laser used is typically a KrF excimer laser, which is often the most expensive component in a PLD system. Some disadvantages of PLD are the phenomenon of splashing and the difficulty in getting large area uniformity. $BaTiO_3$ is grown by PLD typically at conditions of 800°C substrate temperature and oxygen pressure of 2×10^{-3} Torr from a stoichiometric $BaTiO_3$ ceramic target. In 2002, Petraru et al. fabricated $BaTiO_3$ ridge waveguides on MgO single-crystal substrate.[20] The $BaTiO_3$ film was 1-μm thick with a 50-nm-high and 2-μm-wide $BaTiO_3$ ridge patterned in the film. Electrodes were deposited on either side of the ridge to a length of 3 mm separated by a 10-μm gap. For an *a*-axis oriented $BaTiO_3$ film, they reported a V_π of 9.5 V using light with wavelength of 1.55 μm over the 3 mm length ($V_\pi L = 2.85$ V·cm). This implies an effective Pockels coefficient of 45 pm/V. More recently, $BaTiO_3$ was grown by PLD on $DyScO_3$ substrate at 650°C and 1×10^{-2} Torr oxygen pressure by Cao et al.[21] They also patterned and dry-etched the 800-nm $BaTiO_3$ film into a ridge structure with a height of 170 nm and a width of 1.7 μm. While they did not show electro-optic modulation, they showed a very low propagation loss in the waveguide of 2 dB/cm.

Radio frequency (RF) sputtering involves the ejection of atoms from the surface of the source due to a high flux of highly energetic ions impinging on it. The ions knock off atoms from the source by means of kinetic energy transfer. Sputter deposition has many similarities to PLD: it involves the use of a source known as a target and is also able to stoichiometrically transfer the target composition to the growing film under optimized conditions of pressure and target-to-substrate distance. For insulating oxides like $BaTiO_3$, RF sputtering is necessary as DC sputtering does not work. The process gas is also typically a mixture of Ar and O_2. Sputtering is usually performed in the on-axis geometry, which suffers from issues similar to splashing in PLD. A way around this is to use a 90° off-axis geometry that eliminates most of the particulates but at the cost of a greatly reduced growth rate compared to PLD. Rosa et al. grew 50 nm of $BaTiO_3$ by RF sputtering on $SrTiO_3$-buffered SOI wafer with 100 nm of device Si.[22] After growth, the sample was subjected to rapid thermal annealing to improve crystalline quality and oxygenation. RF coplanar waveguides were fabricated to measure the permittivity of $BaTiO_3$ and the propagation losses. More recently, Posadas et al. utilized off-axis RF sputtering to deposit MBE-quality $BaTiO_3$ films at a rate of 2.1 nm/min on Si using a low power density of 2.2 W/cm^2 and a substrate temperature of 700°C using a 30% oxygen in argon mixture at a total pressure of 1×10^{-2} Torr. MZM devices were fabricated on 300-nm films grown on silicon-on-insulator with a 55-nm device Si layer thickness. The waveguides were made using silicon-rich SiN_x with a thickness of 450 nm and the Au/Cr electrodes had a length of 500 μm and a gap of 5.2 μm. The modulators showed a $V_\pi L$ of 0.42 V·cm corresponding to an effective Pockels coefficient of 157 pm/V.[23] Kim also used RF sputtering to grow $BaTiO_3$ on MgO on top of which waveguides were patterned using SiO_x. They used a high sputtering power of 6 W/cm^2 with a 50% oxygen in argon mixture with total pressure of 3×10^{-2} Torr. They formed a 3-μm-wide waveguide with an electrode gap of 80 μm.[24] Their devices showed an effective Pockels coefficient of 110 pm/V and propagation loss of 3–5 dB/cm.

Current state of affairs

To describe the current state of affairs of Si-integrated electro-optic devices, we will start with a more established materials system. Lithium niobate ($LiNbO_3$) or LN is an excellent material for integrated Si photonics. It should be noted however that because it requires energy-intensive and complex wafer bonding and potential wafer size limit of 6 in., LN is only a stop-gap solution. It is transparent in a very wide spectral range from 0.35 to 5 μm and shows strong second order nonlinearity via the Pockels effect.[4] It is a perfect material for EO modulators as it allows pure phase modulation with no variation in absorption. Bulk LN EO devices are extensively used in the telecommunications industry. However, commercial thin-film LN wafers have been developed a few years ago, and the overall performance of thin-film LN modulators is already comparable with the performance of the traditional photonic platforms such as silicon and indium phosphide.[25] Furthermore, thin-film LN EO devices can be integrated on Si. The process is similar to SOI technology: a Czochralski-grown LN wafer is flip-wafer-bonded to an SiO_2 covered Si carrier wafer,[26] then using the smart-cut technology and chemical–mechanical polishing, only a thin device LN film is left on this carrier Si wafer.

There are two main types of LN waveguide modulator designs. When the crystal optical axis is in the plane of the wafer, one talks about an *x*- or *y*-cut, and when the axis is normal to the wafer, one talks about a *z*-cut. Another distinction between waveguide modulators is related to the way the light is guided. Etching techniques are now available to produce waveguides with a very low loss of 0.3 dB/cm, so one can etch

ridge waveguides in LN; these devices are called monolithic.[27] If the waveguide is fabricated in a different high-index guiding material and placed on LN, one talks about hybrid devices.

A decade ago, Lee and co-workers reported hybrid Si-LN resonators fabricated on a silicon-on-insulator platform using a standard 0.18 μm CMOS process.[28] However, the strength of the EO effect was not very high. Using flip-wafer-bonding, Rabiei et al. integrated a thin layer of LNO on Si via wafer bonding with SiO_2 bottom cladding and ridge structures made of Ta_2O_5 deposited on LNO to form ridge waveguides.[26] They demonstrated micro-ring optical resonators and Mach–Zehnder optical modulators. A quality factor of -7.2×10^4 was measured in the micro-resonators, and a half-wave voltage–length product of 4 V·cm and an extinction ratio of 20 dB were measured in the Mach–Zehnder modulators.

Wang and co-authors[29] demonstrated low switching voltage, high bandwidth, and low optical loss in a monolithically integrated LNO modulator with a switching voltage of just 1.4 V, which is a CMOS-compatible drive voltage. It supported data rates up to 210 Gbit/s and showed an on-chip optical loss of less than 0.5 dB. The modulator operated in a traveling wave Mach–Zehnder interferometer configuration. A 20-mm device showed a high 3-dB bandwidth of more than 45 GHz. The devices were fabricated from a commercial *x*-cut LN-on-insulator wafer with a 600-nm device layer on a SiO_2/Si carrier wafer. He et al. used a hybrid LN/Si approach, but the EO effect still occurred in the LN waveguides fabricated by dry etching the *x*-cut LNO membrane.[30] They reported an insertion loss as low as 2.5 dB, EO bandwidth of at least 70 GHz, and modulation rates up to 112 Gbit s^{-1}.

For a comprehensive review of the current state of LN-based Si-integrated modulators we refer the reader to a recent article by Zhang et al.[25] The present and expected all-around performance of these devices is shown in **Figure 1**a, which clearly demonstrates the advantage of a thin-film approach over legacy bulk modulators. These older bulk devices, fabricated in bulk LN crystalline wafers, define optical waveguides by employing proton-exchange or diffusion doping techniques to induce a small perturbation in the refractive index. Long metal electrodes were then placed in close proximity of the waveguide to induce an index change with an externally applied voltage (Figure 1b–c).

In a thin-film LN modulator made from a wavelength-scale optical waveguide, electrodes are placed only a few micrometers from the waveguide with negligible optical absorption loss (Figure 1b–c). At telecom wavelengths (1.55 μm) the voltage–length product $V_\pi \cdot L$ is typically 1.5–3 V cm, which is an order of magnitude lower than in legacy modulators (−15 V cm).[25] To achieve CMOS-compatible drive voltages (1–2 V or lower) thin-film LN modulators can be 1-cm long or less resulting in a larger EO modulation bandwidth beyond 100 GHz, because microwave loss and velocity matching

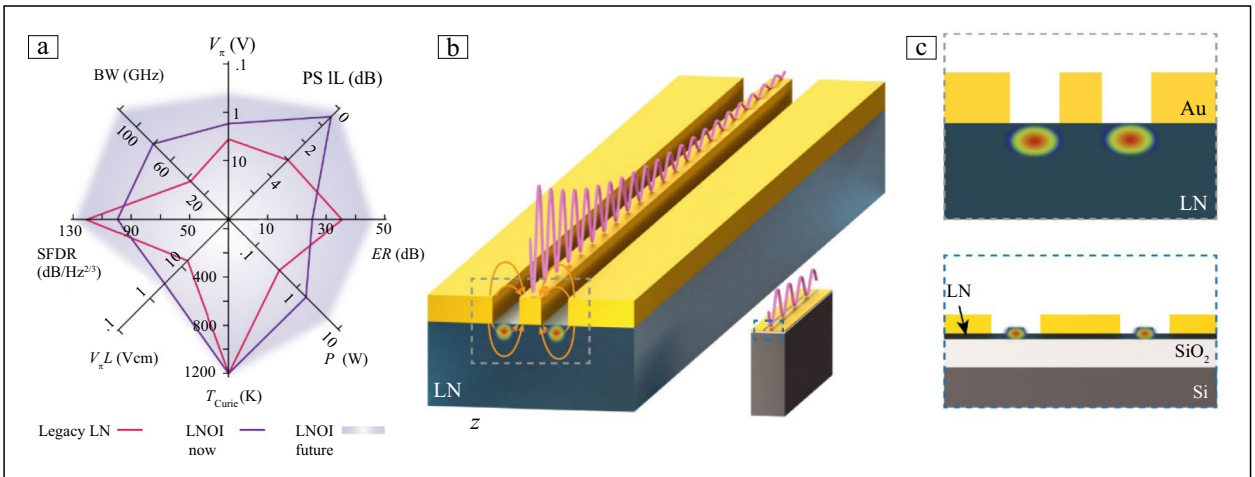

Figure 1. All-around performance and how it is achieved in a thin-film LN platform. (a) Performance octagon of a modulator designed for telecom wavelength. To reflect the engineering trade-space of the modulator, the curves are chosen to circle performance metrics that can possibly be simultaneously achieved as opposed to individually achieved. The red line corresponds to the typical performance of a commercial bulk crystal LN modulator. The purple line shows the performance of a typical integrated thin-film LN modulator. The blue shaded area is the predicted future performance of an optimized thin-film LN modulator. V_π is the half-wave voltage, which characterizes the power consumption; PS IL is the phase shifter insertion loss, which is the excessive loss in modulation areas; BW is the bandwidth, which describes the operation speed; SFDR is the spurious free dynamic range, indicating the modulation linearity and dynamic range; $V_\pi L$ is the product of the half-wave voltage and phase shifter length showing device size and modulation efficiency; T_{Curie} is the glass-transition temperature, which dictates the stability and processability of the electro-optic material; *P* is the optical power handling capability, which is the maximum optical power the modulator can hold; *ER* is the extinction ratio between the on/off states of the modulator. (b) Size comparison of bulk LN devices and thin-film LN devices (aspect ratio not to scale). Longer electrodes usually lead to larger microwave attenuation (purple oscillation) and more challenging velocity matching conditions. (c) Cross section of traditional LN (top) and thin-film LN modulator structures (bottom). Reprinted with permission from Reference 25.

requirements are largely met. The reduced footprint means a dramatically increased packing density: a commercially available 6-in. wafer can accommodate as many as 3000 EO modulators.

The best LN hybrid device performance metrics (taken from different devices) have demonstrated $V_\pi \cdot L$ of 3 V cm, loss as low as 0.2 dB/cm, and bandwidth of 106 GHz, while the monolithic devices boast $V_\pi \cdot L$ of 1.2 V cm, loss of 0.15 dB/cm, and bandwidth 100 GHz.[25]

We now turn to the emerging technology of $BaTiO_3$ that can be easily integrated on Si using direct thin-film deposition techniques, as described above. An early breakthrough in Si-integrated $BaTiO_3$ electro-optic modulators was reported by Xiong et al. in 2014.[31] They fabricated ring resonators and Mach–Zehnder modulators using amorphous Si on top of $BaTiO_3$ grown on SOI wafer. They use a $BaTiO_3$ thickness of 80 nm with an electrode gap of 10 μm and device length of 400 μm for the Mach–Zehnder modulators. The top and bottom Si layers in their structure are both 110-nm thick. They report an effective Pockels coefficient of 213 pm/V, but with relatively high propagation loss of 44 dB/cm and low modulation bandwidth of 0.8 GHz for the Mach–Zehnder devices.

Eltes et al. reported the first low-loss waveguides based on a hybrid $BaTiO_3$-Si structure. Using a strip-loaded waveguide geometry of SiO_2 patterned on top of 50-nm $BaTiO_3$ on SOI with a 100-nm device Si layer, they found that most of the propagation loss in $BaTiO_3$-Si hybrid waveguides are due to hydrogen in the $SrTiO_3$ buffer layer.[32] The propagation losses can be reduced to as low as 2.2 dB/cm by annealing in oxygen for 30 min at 500°C.

In terms of electro-optic modulation at 1.55 μm, the best reported $V_\pi L$ value for a Si-integrated $BaTiO_3$ modulator was reported in 2019 by Eltes et al.[33] They show a value of 0.23 V·cm for a Mach–Zehnder modulator structure with a 1-mm length and an electrode gap of 2.6 μm, which is equivalent to an effective Pockels coefficient of 380 pm/V. Their devices were also shown to be capable of operating at 20 Gbit/s. Rosa et al. have performed RF characterization of $BaTiO_3$ on Si and have shown that MBE-grown films can achieve an electro-optic modulation bandwidth of >40 GHz,[22] but should theoretically be much higher.

Abel et al. showed data rates up to 50 Gbit/s in their hybrid $BaTiO_3$-Si devices based on a Si slot waveguide and ring resonator architecture. The $BaTiO_3$ is 220-nm thick with a 2-μm electrode separation. The Si waveguide is 750-nm wide and 100-nm thick. Their heterostructure also involves wafer bonding as a way to remove Si below the $BaTiO_3$ layer. They report a $V_\pi L$ value of 0.45 V·cm, which based on their reported dn/dV value of 3.4×10^{-4} V^{-1} should correspond to an effective Pockels coefficient of 267 pm/V. Reported losses for these devices are −10 dB/cm.[19]

Reynaud et al. reported on the electro-optic properties of an epitaxially stabilized strained orthorhombic *mm*2 phase of $BaTiO_3$ integrated on Si.[34] Using a thin buffer layer of $BaSnO_3$ to provide a crystalline surface with a lattice constant larger than the *c*-axis lattice parameter of $BaTiO_3$, a tensile-strained orthorhombic phase of $BaTiO_3$ was integrated on Si. With only a thickness of 40 nm, electro-optic modulation using a transmission geometry reveals a decent effective Pockels coefficient of 121 pm/V.

All the previous milestones in the integration of $BaTiO_3$ with Si photonics were made using films grown by MBE. For practical reasons, MBE films are limited to less than 300 nm, and the growth rate is too slow and too unstable for manufacturing. Posadas et al. have reported on a manufacturable process to grow high-quality $BaTiO_3$ films up to 1 μm in thickness.[23] They use off-axis RF magnetron sputtering at low power density (2.2 W/cm^2) in order to achieve film structural quality similar to MBE-grown films, but with 10 times the deposition rate. The process is also very stable from run to run making it amenable to manufacturing. They measured the electro-optic properties of a 300-nm sputtered $BaTiO_3$ film using both transmission geometry and a Mach–Zehnder modulator device. In both cases, they obtain −160 pm/V effective Pockels coefficient, with a $V_\pi L$ value of 0.42 V·cm for the Mach–Zehnder modulator. Their Mach–Zehnder device has a length of 500 μm and an electrode gap of 2.6 μm, with 450-nm SiN_x as the waveguide grown and patterned on top of the $BaTiO_3$ (**Figure 2**a–b). The annular dark-field scanning transmission electron microscope (ADF-STEM) images of the cross section of a 500-nm $BaTiO_3$ film grown at 700°C are shown in Figure 2c–d.

$BaTiO_3$ technology is young, but so far, the results are promising: $V_\pi \cdot L$ of 0.23 V·cm, loss as low as 2.2 dB/cm, and bandwidth >40 GHz have already been demonstrated. Due to a giant Pockels coefficient (up to 900 pm/V[19]) modulators can be very short (−100 μm), potentially offering much higher packing density and lower power than LN devices, in addition to better CMOS compatibility. Integration on an 8-in. wafer is possible and could potentially accommodate as many as 200,000 EO modulators, a significant step-up compared with LN devices.

Applications in computing

Small size and low power of Si-integrated ferroelectric modulators make them attractive for applications in photonic neuromorphic computing. The goal is not to replace conventional computers, but to enable applications that are unreachable or impractical at present by conventional computing, specifically, those that require low latency, high bandwidth, and low energies. The two main reasons that make PICs particularly suited for such implementation are interconnectivity and linear operations.[35] For example, the MZMs can be used in two different ways: a vector MZM representing an SU(2) operator, which can be used in conventional implementations of artificial neural networks; and a scalar MZM that offers nonlinearity, which can be utilized in reservoir computers.[4,36] In **Figure 3** we show a schematic of an EO reservoir architecture based on a single MZM and delay line.[37] This is a machine learning paradigm

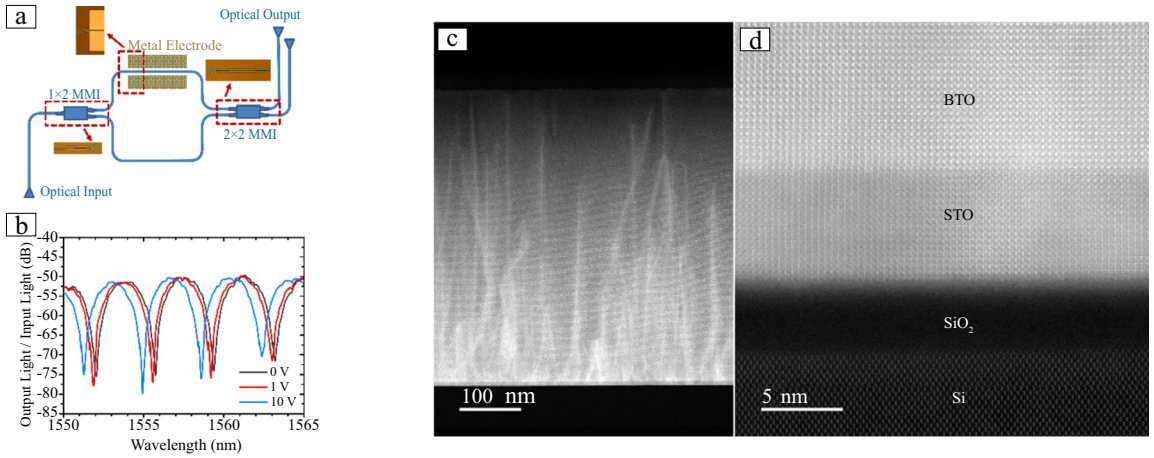

Figure 2. (a) Schematic diagram of the Mach–Zehnder modulator (MZM), with optical microscope images showing 1 × 2 MMI, 2 × 2 MMI, and a section of active region with electrodes. (b) The MZM modulation response under various DC voltages. (c) Low magnification image showing entire $BaTiO_3$ (BTO) layer. The vertical white lines are dislocations. (d) Atomic resolution image of the interface region of the same film. The $BaTiO_3$ and $SrTiO_3$ (STO) are in epitaxial registry. Reprinted with permission from *ACS Appl. Mater. Interfaces* **13**(43), 51230 (2021). © 2021 American Chemical Society.

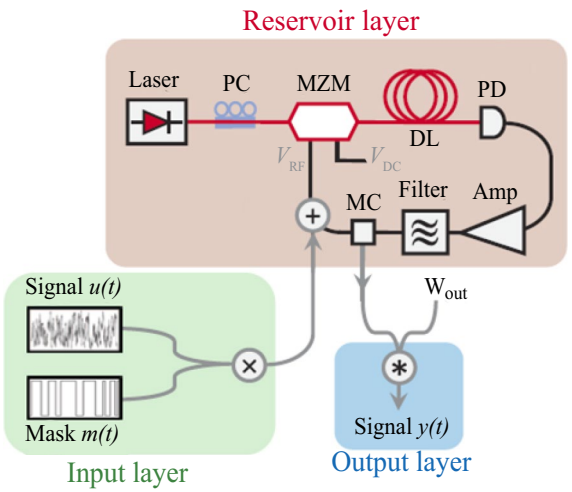

Figure 3. An example of an electro-optic (EO) reservoir computing architecture. The dynamical variable in the feedback loop is $x(t) \propto V_{RF}(t)$, corresponding to the voltage at the radio frequency input of the EO Mach–Zehnder modulator (MZM). PC: polarization controller; DL: delay line; PD: photodiode; Amp: radio frequency amplifier; and MC: microwave coupler. Reprinted with permission from *Chaos* **30**(1), 013111 (2020). © 2020 AIP Publishing.

based on EO oscillators with time-delayed feedback. From the application viewpoint, this architecture leverages the benefits provided by optical and electronic systems: broad bandwidth and controllability. EO reservoirs have already demonstrated results with state-of-the-art performance; the application with the maximum technological readiness is ultrapure microwave generation.[38] A common configuration of EO reservoirs comprises a broadband MZM as a nonlinear element and an optical fiber delay line, both of which can be integrated on Si. A challenge is to demonstrate that they are competitive solutions when considering robustness, size, weight, power, and cost. Silicon photonics with ferroelectric MZMs offers a practical path.

Integrated thin-film LN modulators offer high performance and some potential for scalability. The greatly reduced power consumption and high bandwidth already make them attractive for applications in telecommunications, datacom, and analog photonics. Furthermore, they may provide solutions in quantum photonics, sensing, and artificial intelligence applications. The platform offers sufficient flexibility in design, enabling a combination of performance and circuit complexity. The basic phase modulators have already been used to fabricate a range of fundamental building blocks for complex EO circuits.[25]

By comparison, the $BaTiO_3$ platform is in its infancy. To date, the main thrust has been focused on hybrid *x*-cut devices and more research is needed to develop basic elements. However, the material is promising, first by virtue of its very high Pockels coefficient, and second by having a high-quality but straightforward integration process. Also, monolithic or hybrid *z*-cut devices would allow taking advantage of the anisotropy of the $BaTiO_3$ dielectric tensor and further reduce the driving voltage, leading to even lower power consumption. Recently, a technology has been developed that opens up the way for monolithic $BaTiO_3$ devices. Using ultrathin body SOI wafers, Ortmann et al. were able to completely eliminate the device Si layer after the $SrTiO_3$ buffer has been deposited[39,40] using a Deal–Grove-type oxidation at the buried interface.[41] The microscopic images of this process are shown in **Figure 4**a–b. The $BaTiO_3$ layer can be fabricated on top of this crystal-on-glass (COG) substrate by a number of

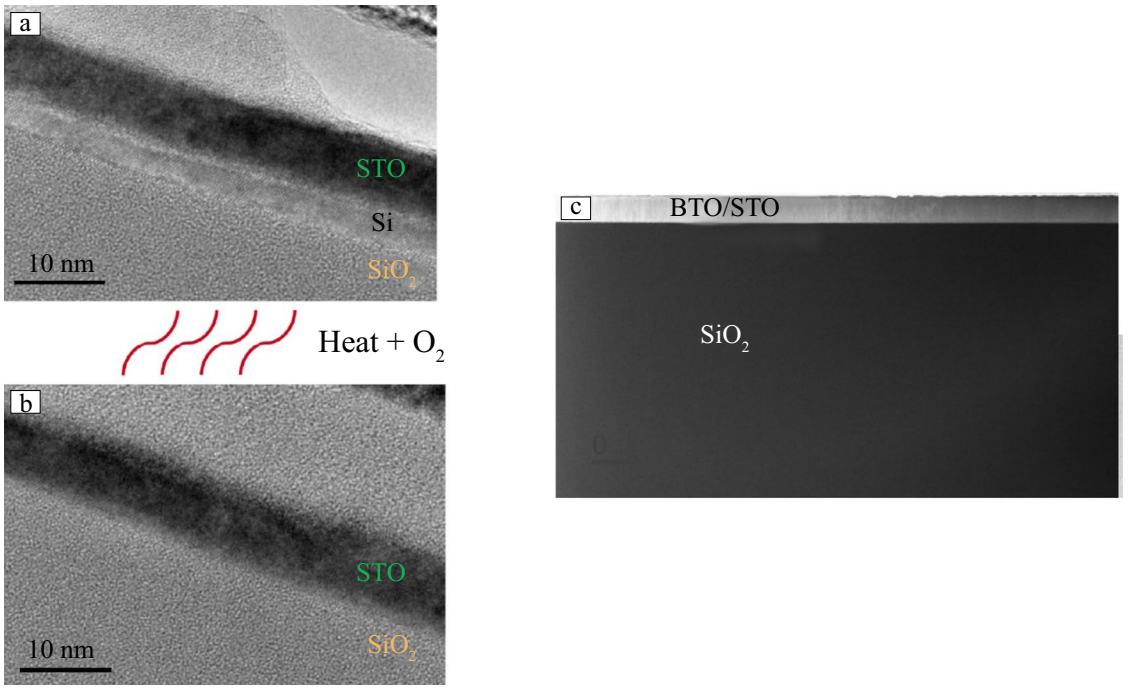

Figure 4. (a) An $SrTiO_3$ (STO) buffer layer grown on ultrathin body silicon-on-insulator (SOI) wafer. (b) Dry oxidation is used to eliminate the Si device layer. (c) 100 nm of $BaTiO_3$ (BTO) is deposited by radio frequency sputtering on the STO buffer resulting in fabrication of BTO directly on the buried oxide (BOX) layer of an SOI wafer. Reprinted with permission from *ACS Appl. Nano Mater.* **2**(12), 7713 (2019). © 2019 American Chemical Society.

deposition techniques. In Figure 4c, we show a 100-nm-thick $BaTiO_3$ layer grown by RF sputtering. This approach enables the easy fabrication of $BaTiO_3$ on insulator wafers similar to $LiNbO_3$-on-insulator (LNOI) wafers without the need for wafer-bonding processes beyond what is already used in commercial SOI technology.

In conclusion, ferroelectrics exhibiting robust linear electro-optic effect can enable significant reduction in the size and power requirements of EO modulators integrated on silicon. The use of neuromorphic algorithms allows for these relatively large devices to be competitive with conventional silicon electronics that are based on von Neumann architecture, and at the same time, leverage the existing CMOS manufacturing infrastructure.

Acknowledgments

This work was supported by the Air Force Office of Scientific Research under Award No. FA9550-18-1-0053.

Conflict of interest

On behalf of all authors, the corresponding author states that there is no conflict of interest.

References

1. M. Waldrop, *Nature* **530**, 147 (2016)
2. K. Yamada, Y. Urino, T. Nakamura, Y. Arakawa, *NTT Tech. Rev.* **11**, 1 (2013)
3. P. Stark, F. Horst, R. Dangel, J. Weiss, B.J. Offrein, *Nanophotonics* **9**, 4221 (2020)
4. A.A. Demkov, C. Bajaj, J.G. Ekerdt, C.J. Palmström, S.J. Ben Yoo, *J. Appl. Phys.* **130**, 1070907 (2021)
5. G. Sinatkas, T. Christopoulos, O. Tsilipakos, E.E. Kriezis, *J. Appl. Phys.* **130**, 010901 (2021)
6. A. Rahim, A. Hermans, B. Wohlfeil, D. Petousi, B. Kuyken, D. Van Thourhout, R. Baetsa, *Adv. Photonics* **3**, 024003 (2021)
7. R.A. McKee, F.J. Walker, M.F. Chisholm, *Phys. Rev. Lett.* **81**, 3014 (1998)
8. J.W. Reiner, A.M. Kolpak, Y. Segal, K.F. Garrity, S. Ismail-Beigi, C.H. Ahn, F.J. Walker, *Adv. Mater.* **22**, 2919 (2010)
9. D. Diaz-Fernandez, M. Spreitzer, T. Parkelj, D. Suvorov, *Appl. Surf. Sci.* **455**, 227 (2018)
10. A.C. Jones, M. Hitchman, Eds., *Chemical Vapor Deposition: Precursors, Processes, and Applications* (RSC Publishing, Cambridge, 2009)
11. D.J. Towner, J. Ni, T.J. Marks, B.W. Wessels, *J. Cryst. Growth* **255**, 107 (2003)
12. P. Tang, D.J. Towner, A.L. Meier, B.W. Wessels, *Appl. Phys. Lett.* **85**, 4615 (2004)
13. T.Q. Ngo, A.B. Posadas, M.D. McDaniel, C. Hu, J. Bruley, E.T. Yu, A.A. Demkov, J.G. Ekerdt, *Appl. Phys. Lett.* **104**, 082910 (2014)
14. E.L. Lin, A.B. Posadas, L. Zheng, J. Elliott Ortmann, S. Abel, J. Fompeyrine, K. Lai, A.A. Demkov, J.G. Ekerdt, *J. Appl. Phys.* **126**, 064101 (2019)
15. J.H. Qiu, J.N. Ding, N.Y. Yuan, X.Q. Wang, Y. Zhou, *Solid State Commun.* **151**, 1344 (2011)
16. I. Chilibon, J.N. Marat-Mendes, *J. Solgel Sci. Technol.* **64**, 571 (2012)
17. B.I. Edmondson, S. Kwon, J.E. Ortmann, A.A. Demkov, M.J. Kim, J.G. Ekerdt, *J. Am. Ceram. Soc.* **103**, 5700 (2020)
18. M. Henini, Ed., *Molecular Beam Epitaxy: From Research To Mass Production* (Elsevier, Oxford, 2013)
19. S. Abel, F. Eltes, J.E. Ortmann, A. Messner, P. Castera, T. Wagner, D. Urbonas, A. Rosa, A.M. Gutierrez, D. Tulli, P. Ma, B. Baeuerle, A. Josten, W. Heni, D. Caimi, L.

Czornomaz, A.A. Demkov, J. Leuthold, P. Sanchis, J. Fompeyrine, *Nat. Mater.* **18**, 42 (2018)
20. A. Petraru, J. Schubert, M. Schmid, Ch. Buchal, *Appl. Phys. Lett.* **81**, 1375 (2002)
21. Y. Cao, S.L. Tan, E.J.H. Cheung, S.Y. Siew, C. Li, Y. Liu, C.S. Tang, M. Lal, G. Chen, K. Dogheche, P. Yang, S. Pennycook, A.T.S. Wee, S. Chua, E. Dogheche, T. Venkatesan, A. Danner, *Adv. Mater.* **33**, 2101128 (2021)
22. A. Rosa, D. Tulli, P. Castera, A.M. Gutierrez, A. Griol, M. Baquero, B. Vilquin, F. Eltes, S. Abel, J. Fompeyrine, P. Sanchis, *Opt. Mater. Express* **7**, 4328 (2017)
23. A.B. Posadas, H. Park, M. Reynaud, W. Cao, J.D. Reynolds, W. Guo, V. Jeyaselvan, I. Beskin, G.Z. Mashanovich, J.H. Warner, A.A. Demkov, *ACS Appl. Mater. Interfaces* **13**, 51230 (2021)
24. I.-D. Kim, Y. Avrahami, L. Socci, F. Lopez-Royo, H.L. Tuller, *J. Asian Ceram. Soc.* **2**, 231 (2014)
25. M. Zhang, C. Wang, P. Kharel, D. Zhu, M. Lončar, *Optica* **8**, 652 (2021)
26. P. Rabiei, J. Ma, S. Khan, J. Chiles, S. Fathpour, *Opt. Express* **21**, 25573 (2013)
27. M. Zhang, C. Wang, R. Cheng, A. Shams-Ansari, M. Lončar, *Optica* **4**, 1536 (2017)
28. Y.S. Lee, G.D. Kim, W.J. Kim, S.S. Lee, W.G. Lee, W.H. Steier, *Opt. Lett.* **36**, 1119 (2011)
29. C. Wang, M. Zhang, X. Chen, M. Bertrand, A. Shams-Ansari, S. Chandrasekhar, P. Winzer, M. Lončar, *Nature* **562**, 101 (2018)
30. M. He, M. Xu, Y. Ren, J. Jian, Z. Ruan, Y. Xu, S. Gao, S. Sun, X. Wen, L. Zhou, L. Liu, C. Guo, H. Chen, S. Yu, L. Liu, X. Cai, *Nat. Photonics* **13**, 359 (2019)
31. C. Xiong, W.H.P. Pernice, J.H. Ngai, J.W. Reiner, D. Kumah, F.J. Walker, C.H. Ahn, H.X. Tang, *Nano Lett.* **14**, 1419 (2014)
32. F. Eltes, D. Caimi, F. Fallegger, M. Sousa, E. O'Connor, M.D. Rossell, B. Offrein, J. Fompeyrine, S. Abel, *ACS Photonics* **3**, 1698 (2016)
33. F. Eltes, C. Mai, D. Caimi, M. Kroh, Y. Popoff, G. Winzer, D. Petousi, S. Lischke, J.E. Ortmann, L. Czornomaz, L. Zimmermann, J. Fompeyrine, S. Abel, *J. Lightwave Technol.* **37**, 1456 (2019)
34. M. Reynaud, P.-Y. Chen, W. Li, T. Paoletta, S. Kwon, D.H. Lee, I. Beskin, A.B. Posadas, M.J. Kim, C.M. Landis, K. Lai, J.G. Ekerdt, A.A. Demkov, *Phys. Rev. Mater.* **5**, 035201 (2021)
35. B.J. Shastri, A.N. Tait, T. Ferreira de Lima, W.H.P. Pernice, H. Bhaskaran, C.D. Wright, P.R. Prucnal, *Nat. Photonics* **15**, 102 (2021)
36. Y. Paquot, F. Duport, A. Smerieri, J. Dambre, B. Schrauwen, M. Haelterman, S. Massar, *Sci. Rep.* **2**, 287 (2012)
37. Y.K. Chembo, *Chaos* **30**(1), 013111 (2020)
38. Y.K. Chembo, D. Brunner, M. Jacquot, L. Larger, *Rev. Mod. Phys.* **91**, 035006 (2019)
39. J.E. Ortmann, A.Y. Borisevich, S. Kwon, A. Posadas, M.J. Kim, A.A. Demkov, *ACS Appl. Nano Mater.* **4**(2), 2153 (2021)
40. J.E. Ortmann, M.R. McCartney, A. Posadas, D.J. Smith, A.A. Demkov, *ACS Appl. Nano Mater.* **2**(12), 7713 (2019)
41. W. Guo, A.B. Posadas, A.A. Demkov, *J. Appl. Phys.* **127**, 055302 (2020) □

Alexander A. Demkov is professor of physics at The University of Texas at Austin. He earned his Diploma in materials science from the Moscow Institute of Steel and Alloys in 1986, and PhD degree in theoretical condensed-matter physics from Arizona State University in 1995. He joined The University of Texas in 2005, after working in Motorola's R&D organization, where he investigated materials-related problems of electronic devices making significant contributions to the understanding of high dielectric constant materials. His current research is focused on transition-metal oxides integrated with semiconductors. He researches both theory and oxide molecular beam epitaxy. Demkov can be reached by email at demkov@physics.utexas.edu.

Agham B. Posadas is managing the Oxide MBE lab at The University of Texas at Austin. He received his PhD degree in applied physics from Yale University in 2007, his MS degree in materials science and engineering (in 1997), and BS degree in applied physics (in 1994) from the University of the Philippines. His prior scientific work includes bulk growth and characterization of high-T_c superconductors at the University of the Philippines, and fabrication of Si and SiGe heterostructures using molecular beam epitaxy (MBE) as a research student at The University of Tokyo. At Yale, his doctoral research involved the growth and characterization of functional oxide thin films on semiconductors using both RF sputtering and MBE. Posadas also has expertise in magnetic and transport measurements as well as in thin-film crystallographic characterization using four-circle x-ray diffractometry. He joined The University of Texas at Austin in 2009 becoming one of the principal researchers in the new Materials Physics Laboratory. He has co-authored more than 70 research papers on various oxide thin-film heterostructures, several book chapters, and a book on the integration of oxides with semiconductors.